SAND2022-5111C

Pressure and Strain Measurement on a 10° Flap of a Slender Cone in Hypersonic Flow

Amruthkiran Hegde[1], Zach MacIntyre[2], and James P. Hubner[3]
The University of Alabama, Tuscaloosa, AL 35401

Mingtai Chen[4]
North Carolina State University, Raleigh, NC 27607

Anshuman Pandey[5], John Flood[6], and Katya M. Casper[7]
Sandia National Laboratories, Albuquerque, NM 87185

This paper presents the results of an experimental technique to acquire full-field pressure and strain fields on the windward side of a 10° flap attached to a slender cone-slice model. Tests were conducted in the Hypersonic Wind Tunnel ($M = 5$, $Re = 9 - 14 \times 10^6$/m, air) at Sandia National Laboratories. The flap was coated with a fast-response, pressure-sensitive paint sprayed over a photoelastic coating and located near the trailing-edge of an axial slice along the 7° slender cone. This experiment was part of a sponsored project to develop the two-coating luminescent measurement technique and apply to high-speed, fluid-structure interaction environments. Results using a low-speed micropolarizer camera with four polarization orientations show that the technique is sensitive to pressure and strain, measuring an increasing pressure and decreasing strain from leading- to trailing-edge over the surface of the flap. At the low Re condition, the pressure signal captures the separated region near the flap leading edge and compares well with schlieren and oil-film measurements, the latter on a 10° wedge. Aerodynamic heating during the run does affect the pressure signal, likely resulting in an overestimation of pressure. Results using a conventional high-speed camera with a single linear polarizer captures the first bending and torsional modes of vibration when the flap is excited by transient shutdown conditions; however, coupling is difficult to detect in the pressure response due to baseline noise and the slower temporal response of the pressure coating.

Nomenclature

Variables

A, B = PSP calibration coefficients
E = modulus of elasticity
h = coating thickness
I = emission intensity
k = thermal conductivity
K = optical sensitivity
L = cantilever flap length
N = fringe order
P = pressure
t = time

Abbreviations

LP = linear polarizer
HPF = high-pass filter
HWT = hypersonic wind tunnel
JCEAP = joint comp/exp aerodynamics program
OSR = optical strain response
PEC = photoelastic coating
PSP = pressure-sensitive paint
QWP = quarter-wave plate
SWBLI = shock-wave boundary-layer interaction
TSP = temperature-sensitive paint

[1] Graduate Student, Aerospace Engineering and Mechanics, AIAA Member
[2] Former Graduate Student, Aerospace Engineering and Mechanics; currently at NASA JPL
[3] Professor, Aerospace Engineering and Mechanics, AIAA Associate Fellow
[4] Assistant Teaching Professor, Aerospace Engineering, AIAA Young Professional Member
[5] Postdoctoral Researcher, Engineering Science Center, AIAA Member
[6] Graduate Student Intern, Engineering Science Center, AIAA Member
[7] Principal Member of the Technical Staff, Engineering Science Center, AIAA Associate Fellow

T = temperature
α = analyzer angle
α_T = thermal diffusivity
γ = maximum in-plane shear strain
η = strain calibration coefficient
λ = wavelength
θ = principal strain direction
σ = standard deviation
τ = PSP temperature sensitivity parameter
ϕ = polarization efficiency

Superscripts and Subscripts
$( )^*$ = ratio relative to atmospheric condition
$( )_o$ = stagnation
$( )_b$ = blue (PSP) excitation
$( )_r$ = red (PEC) excitation

I. Introduction

This paper presents the application of two full-field, optical sensor techniques to measure the unsteady, distributed loads (pressure) and strains on aerodynamic surfaces in high-speed flows where vibrations and aero-thermal loading are important. The approach is to combine fast-response pressure sensitive paint (PSP) [1,2] with a thin photoelastic coating (PEC) [3] to create a fast luminescent pressure and strain measurement technique [4,5]. The technique was tested on a model in the Sandia National Laboratories Mach 5 Hypersonic Wind Tunnel (HWT-5). The model was a sharp-nosed cone with a 7° half-angle and a base diameter of 127 mm. A longitudinal slice extends 144.8 mm upstream from the base of the cone. The cone-slice geometry is inspired by the geometries used in the Maneuvering Aerothermal Technology program [6] and the Joint Computational/Experimental Aerodynamics Program (JCEAP) [7]. In supersonic and hypersonic flows, inclined surfaces are exposed to phenomena such as shock-wave boundary-layer interactions (SWBLI) [8-10]. This in turn can lead to dynamic pressure and deformation fields arising from transient mechanical loads due to oscillating shock fronts and separating vortices that can potentially couple with structural resonant frequencies.

In recent Sandia studies on a JCEAP-inspired model [11,12], wedges of varying inclination angles ($10° - 30°$) were investigated. The extent of SWBLI was dependent on the flow Reynolds number (Re). Figure 1 shows oil-film surface visualization results over a 10° wedge. In the lower Re case (Fig. 1b) the incoming boundary layer is laminar and separates from the slice upstream of the wedge leading edge. At the higher Re case (Fig. 1c), the boundary layer is turbulent over the slice and remains attached at the wedge leading edge.

In the experiment presented in this paper, the wedge and clamped-plate configuration was replaced with a cantilever flap. The flap lowers the fundamental frequency compared to the clamped-plate and creates a decreasing strain gradient across the length of the flap. A 10° tempered aluminum-alloy flap (58 mm long on the windward side, 2 mm thick) was installed at the aft end of the cone-slice model (Fig. 2). The 10°-flap angle was selected considering tunnel safety and to reduce thermal loading. A similar upstream flow environment relative to Re based on prior 10°-

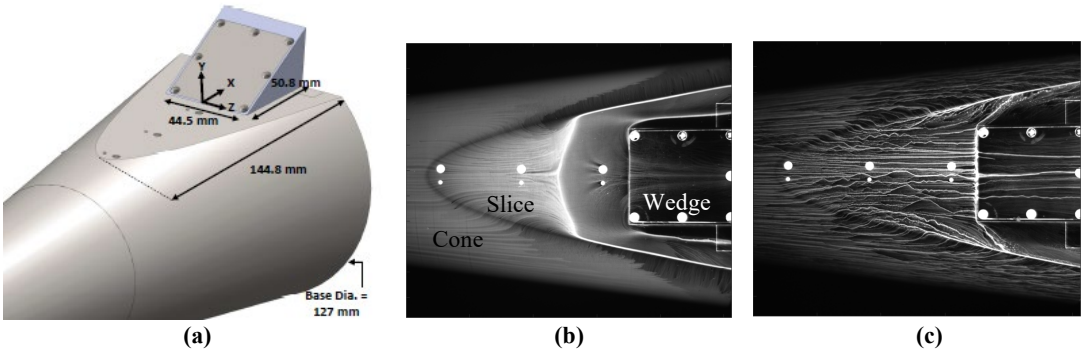

Figure 1. Cone-slice-wedge model and top-view oil-film surface visualization images: (a) isometric view [11,12], (b) $Re = 3.5 \times 10^6/\text{m}$, boundary layer is separated, and (c) $Re = 15.8 \times 10^6/\text{m}$, boundary layer is attached; flow is left-to-right

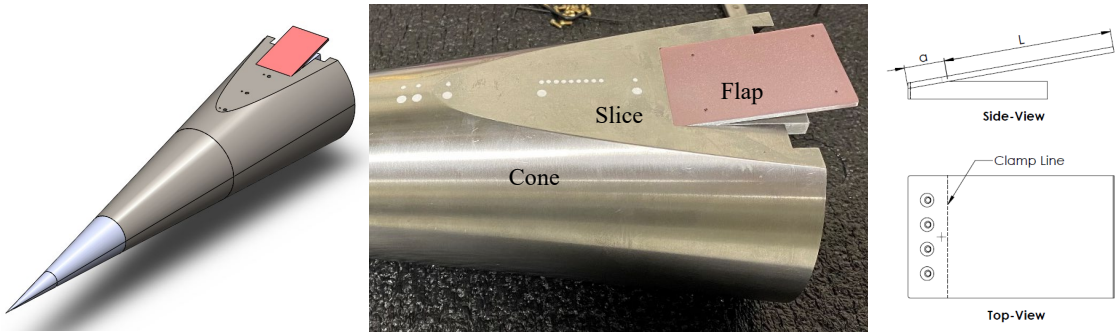

Figure 2. Cone-slice-flap geometry: (a) isometric view, (b) image of the flap installed in the model (the PSP creates the pink hue), and (c) schematic of the flap with dimensions, $a = 7$ mm, $L = 51$ mm, and thickness $= 2$ mm

wedge experiments is expected for the flap. The flap configuration was tested over a range of Re $(9 - 14 \times 10^6/\mathrm{m})$ to generate transitional and turbulent boundary layers upstream of the flap. The following sections cover the technique, equipment, results and discussion of experimental data.

II. Technique Theory

The combined coating technique uses a PSP sprayed on top of a PEC (more details regarding the two coatings are presented in Section III), enabling oxygen quenching of the PSP and creating a luminescent pressure and strain sensitive coating. Figure 3 is a schematic of the excitation, emission, and reflection concept. The coating is alternately excited with red circular-polarized light and blue/UV (appropriate PSP absorption band) unpolarized light. The PSP is of sufficient thickness to enable the red excitation to doubly pass through the PEC coating, reflecting off the surface. A high-pass (or bandpass) optical filter is used to block the PSP excitation and allow both the unpolarized PSP emission and the polarized PEC reflection to pass to the camera. The intensity is captured through a pixelated polarizer mounted on the imaging sensor. Each pixel acquires an intensity relative to the polarization orientation of that pixel. The micropolarizer array has four discrete orientations in a 2×2 pattern: $0/45/90/135°$. The group of four pixels is called a superpixel.

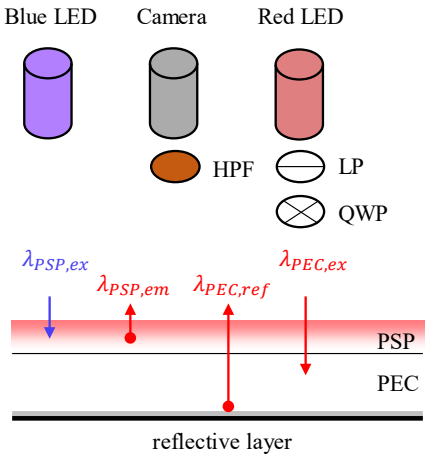

Figure 3. Emission and reflection paths for the PSP and PEC, respectively

The pressure information is tracked by the average of the four pixel intensities (assuming strain-independence) from the PSP emission, and the strain information is modeled by the variance of the pixel intensities (assuming pressure-independence) from the PEC reflection. For a superpixel exposed to the blue LED,

$$\bar{I}_b = \frac{\Sigma I_{b,\alpha}}{4} \tag{1}$$

where α represents each of the four polarization orientations. In terms of the Stern-Volmer pressure response,

$$\frac{\overline{I_{b,ref}}}{\bar{I}_b} = A + B\frac{P}{P_{ref}} \tag{2}$$

where A and B are temperature sensitive. The strain response for the two-layer coating exposed to the red LED is modeled by

$$\frac{I_{r,\alpha}}{\overline{I_{r,\alpha}}} = 1 + \phi \sin\left(\frac{\gamma}{\eta}\right)\sin(2\alpha - 2G)\,, \tag{3}$$

where $I_{r,\alpha}$ is the intensity of each pixel polarization. Polarization efficiency, ϕ, can account for attenuation effects such as the depolarization of excitation and non-ideal polarization extinction ratio of the camera pixels. Relative to the pixel orientation, α, the measured intensity follows a sinusoidal curve $\sin(2\alpha - 2G)$. The amplitude of the corresponding curve fit, or the OSR, is $\phi\sin(\gamma/\eta)$. To calculate OSR and the phase, and hence strain and principal direction, a non-linear fit algorithm such as the Levenberg-Marquart routine is suitable. Alternatively, and more computationally efficient, the standard deviation of $\frac{I_{r,\alpha}}{\overline{I_{r,\alpha}}}$ for a superpixel can be used,

$$\mathrm{OSR} = \phi\sin\left(\frac{\gamma}{\eta}\right) = \sqrt{\frac{n-1}{n}}\,\mathrm{stdev}\left(\frac{I_{r,\alpha}}{\overline{I_{r,\alpha}}}\right), \tag{4}$$

where n is the number of evenly spaced pixel orientations (in this case $n = 4$). To calculate the phase,

$$2G = \mathrm{atan2}\left(\frac{I_0 - I_{90}}{I_{45} - I_{135}}\right). \tag{5}$$

and is dependent on the clockwise or counter-clockwise orientation of the circular polarized excitation. In cases where the strain is zero or at a fringe node, the intensity ratio is theoretically constant with respect to analyzer orientation and $\mathrm{OSR} = 0$. If the OSR is not zero at the reference state (e.g., residual birefringence in the coating), then a vector subtraction of the residual state is necessary. This correction process is further discussed in Ref. 4.

When calculating the corresponding strain from the measured OSR, multiple strain values could result. This requires fringe counting or phase unwrapping. By limiting the coating thickness to less than a quarter-fringe, fringe counting is eliminated. The fringe order, N, is

$$N = \frac{\gamma}{2\pi\eta}\,. \tag{10}$$

This corresponds to $N < \frac{1}{4}$ or $\gamma_{max} < \frac{\lambda_r}{8hK}$ as well as knowledge *a priori* of the expected maximum shear strain.

III. Instrumentation and Experiment

The Sandia HWT is a conventional blowdown-to-vacuum facility. The tunnel employs an interchangeable system of nozzles and heater sections which enables the Mach number in the test section to be set at 5, 8 or 14. In this work, the experiments were conducted at Mach 5 which uses air for the flow environment and is necessary for PSP measurements. Typical runs were about 30-35 seconds long, with an initial rise in stagnation pressure followed by a rise in stagnation temperature until target conditions were achieved for each run. The Mach 5 configuration has a stagnation pressure range of $345 - 1380$ kPa and a stagnation temperature range of $330 - 890$ K, providing a Reynolds number range of $3 - 26 \times 10^6$/m. Noise levels (Pitot pressure fluctuations over the mean Pitot pressure) vary from $1 - 2\%$.

Prior to testing, estimates of the flap strain were calculated based on tunnel start-up/shut-down loads, material properties, cantilever beam theory, and compressible flow theory in order to set the maximum tunnel stagnation pressure for the experiment. For Mach 5 flow, oblique shock (axisymmetric for the cone and two-dimensional for the flap) and expansion wave (two dimensional) theory was used to calculate a first-order estimate of the upper (windward) surface pressure of the flap: $P_o/P_{flap} = 226$. For the purposes of the estimate, the upper surface pressure distribution was assumed uniform and the lower (leeward) surface pressure was assumed zero, adding to the safety margin. Based on expected start-up/shut-down loading data provided by Sandia and a 3X safety factor, the maximum stagnation pressure was restricted to 910 kPa. The maximum stagnation pressure tested was 760 kPa, and the estimated steady-state and start-up/shut-down maximum principal strains are 94 and 1110 με, respectively, well below the yield strength of the flap. Longer or higher angled flaps were considered but would be exposed to larger base strains and higher aerodynamic heating, requiring lower stagnation pressures. To test within the transitional Re range, target conditions for the experiments were set at $480 - 760$ kPa and 410 K ($Re = 9 - 14 \times 10^6$/m); these run conditions are indicated on the left-side of the tunnel test envelope shown in Fig. 4.

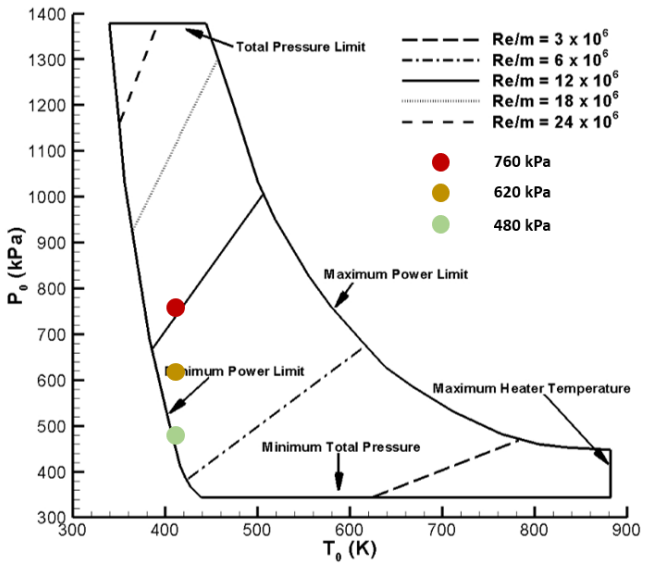

Figure 4. HWT-5 stagnation pressure and temperature test envelope with three target test conditions indicated

The flap and baseplate assembly was fabricated from aluminum alloy 6061-T6. The baseplate was designed to mount into the cone-slice model and incline the flap at 10° (Fig. 2). The windward side of the flap is 58 mm, creating a 51 mm cantilever length on the leeward side of the flap. The flap is 2 mm thick and 44.5 mm wide. It was attached to the baseplate with four 2-56 countersunk bolts and thread-locking adhesive. An epoxy was applied on top of the bolt heads and then sanded to create a smooth surface. The surface was then cleaned and prepared for the application of the PEC (Micro-Measurement's PS-1D; $h = 0.51\ mm$). The PEC was adhered to the flap utilizing PC-10C adhesive [13]. After applying the PEC, the specimens were sent to ISSI to apply a custom formulation of PtTFPP PSP [14]. First, a water-based polymer formulation was sprayed onto the PEC. This underlayer assists in protecting the PEC from the solvents of the PSP layer. The polymer included a small volume of a low refraction index porous media

instead of traditionally used titanium dioxide. Increasing the concentration of the porous media diminishes the polarization retention of the signal. A thin layer of PtTFPP was sprayed on the surface of the polymer until a light-pink hue of the PSP was visible, balancing between the signal strength of the PSP and PEC. Temporal response of the pressure signal of the formulation was measured at 2 ms using a calibration shock tube at ISSI. The center absorption band of the PSP is approximately 400 nm, and the center emission band is near 650 nm.

The structural response of the specimen is partially affected by the coating. The resulting strain measurement is a function of coating-to-specimen thickness ratio, coating-to-specimen modulus of elasticity ratio, and the type of load (in- or out-of-plane deformation) [15]. For the PEC coated flap specimen, $h_{PEC}/h_{flap} = 0.25$ and $E_{PEC}/E_{flap} = 0.04$. As the load in this application is primarily bending in nature, the corresponding correction factor was 0.86. An *a priori* calibration was used [4]. The effect on the fundamental resonant frequency of the flap was assessed by testing the response of a companion specimen first without and then with the coating. The coating increased the resonance frequency from 439 Hz to 538 Hz. Specimen to specimen resonance frequency can fluctuate based on the torque of the attachment bolts and differences between the specimen geometry.

The optical set-up (Fig. 5b) consisted of an air-cooled ISSI LM3X 405 nm (blue/UV, PSP) LED lamp and a water-cooled ISSI LM2X 620 nm (red, PEC) LED lamp. A linear polarizer and an achromatic QWP, rotated at 45° relative to the polarizer, were aligned with the red LED to create circular polarized light. The LEDs were triggered alternately using SRS digital generators triggered on tunnel start conditions. The images were acquired at 160 fps using a 4D-Technologies PolarCam U2 CMOS camera with a micropolarizer mask (0/45/90/135° superpixel orientations). Because the red and blue LED were sequentially strobed, the effective rate was 80 fps. This was suitable to detect time-dependent trends due to the rise and fall from tunnel target conditions but not the resonance modes of the flap. Additional tests were performed using a Phantom v2512 camera at 5000 fps to detect flap vibration induced by tunnel shutdown. The Phantom camera does not have a polarization mask with multiple polarization angles. Thus, while strain cannot be directly measured, the vibrational response of the flap can be measured when a single polarizer is placed appropriately in the optical path to detect modification of polarized excitation. Both cameras used a Nikon 50 mm lens set at an f-stop of 1.2. A 450 nm reflective HPF and a 570 nm Schott glass HPF were attached to the lens.

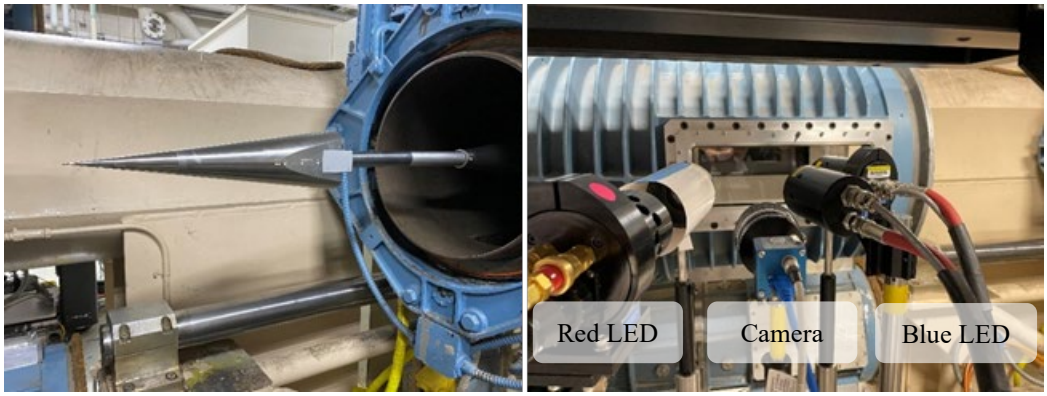

Figure 5. Images of HWT-5 set-up: (a) the cone-slice-flap model attached to the tunnel sting and (b) LED/camera test equipment outside the test section window

High-speed schlieren tests were also separately performed on the flap model. The model was rotated 90° relative to the PSP/PEC tests to create an optical path through the test section windows and over the flap. The light source was a red LED (SugarCUBE) that provided continuous illumination. The z-type schlieren configuration used two 450.8 mm diameter spherical mirrors for light-collimation. The knife edge was oriented horizontally (parallel to the slice) and the high-speed v2512 camera captured the density gradients in the flow field at 40 kHz. A 150 mm lens was placed in front of the camera to provide 1024×304 pixel resolution images of the slice-flap region.

IV. Results and Discussion

A. Micropolarizer Camera Results

As discussed in the previous section, experiments were conducted at three nominal Re test conditions. After installing the model and closing the test section, reference images were captured at ambient (atmospheric) conditions: nominally $82.7\ kPa$ and $297\ K$. Then the tunnel vacuum valve was opened to evacuate the test section. A second reference image was captured after the test section temperature equilibrated. These first two images enabled a calibration of the pressure coating at ambient temperature conditions.

To initiate the tunnel run, first the data acquisition system was started, shortly followed by opening the stagnation pressure valve and finally powering the tunnel heaters to reach the target freestream condition. Figures 6a&b display

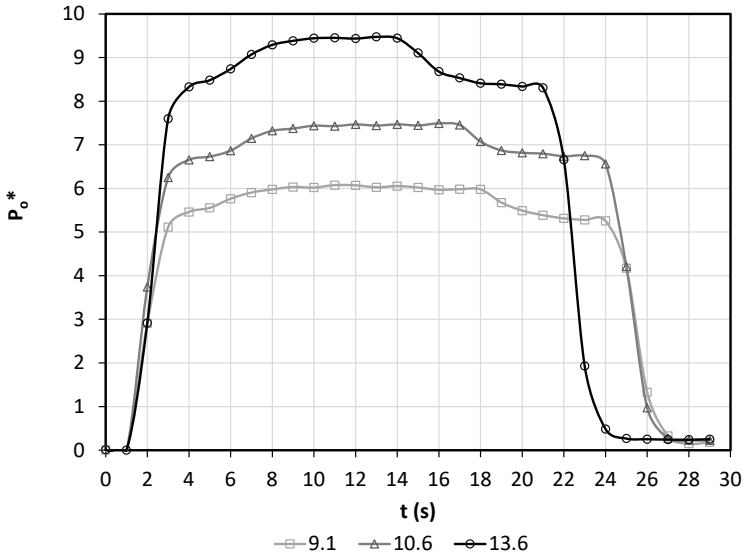

(a)

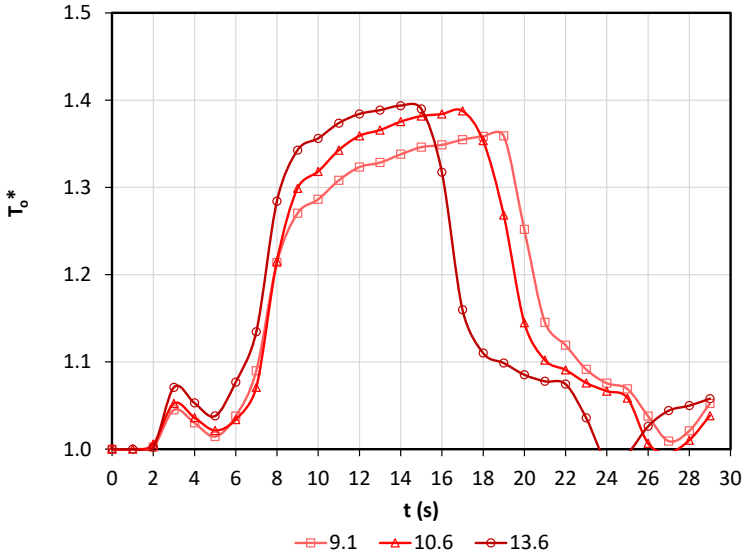

(b)

Figure 6. Tunnel stagnation traces relative to pre-run atmospheric conditions for three Re settings: $9.1, 10.6$ and $13.6 \times 10^6/\mathrm{m}$: (a) stagnation pressure and (b) stagnation temperature

the stagnation pressure and temperature rise, respectively, for three runs that used the micropolarizer camera. Both pressure and temperature are plotted relative to pre-run atmospheric tunnel pressure and temperature. About 1 s after the data acquisition was started, the pressure valve was opened. Due to the expansion and corresponding low stagnation and static temperatures, condensate and non-isentropic flow exists. After the initial pressure rise, at approximately 5 s, the heaters were energized. As shown in Fig. 6a, an additional bump appears in the stagnation pressure as the stagnation temperature sharply increases. Target flow conditions were reached over the next $3-4$ s and held constant for the rest of the run duration. During this time, there was a moderate stagnation temperature increase while the stagnation pressure holds steady. For these tests, conditions were held for $6-10\ s$ and then the heaters were turned off followed by the closing of the tunnel pressure control valve. While closing the valve, the tunnel unstarts and causes transient model loading.

Figure 7 displays uncorrected pressure ratio and optical strain response at 12 s for each run case. The pressure ratio contours show lower pressure near the leading edge and center of the flap. This is particularly pronounced for the lowest Re case, indicating a separation region upstream of the flap. For higher stagnation pressures, the pressure increases and the separation region size decreases as the boundary layer remains attached along the cone-slice up to the leading-edge of the flap. The OSR response shows higher strains at the clamp line and decreasing towards the trailing edge, typical of a distributed pressure load along a cantilever beam or plate. The white tick marks in the OSR results mark the principal strain direction and indicate bending along the longitudinal axis. Figure 8 shows an overlay of the pressure contours onto surface oil-film results of a $10°$ wedge tested at similar Re. The width of the low pressure region indicated by the pressure contour corresponds with the small separation region upstream of the wedge leading edge. This separation region decreases as Re is increased. The separation region is also captured in schlieren images of the flow (separate runs at same Re) shown in Figure 9. The sharp gradient produced by the separation shock is visible and appears to emanate further upstream at higher Re in accordance with the separation region obtained from the PSP results. Also visible in the schlieren images are the expansion waves at the trailing edge of the flap. These images indicate consistent separation locations to both the oil flow and PSP measurements.

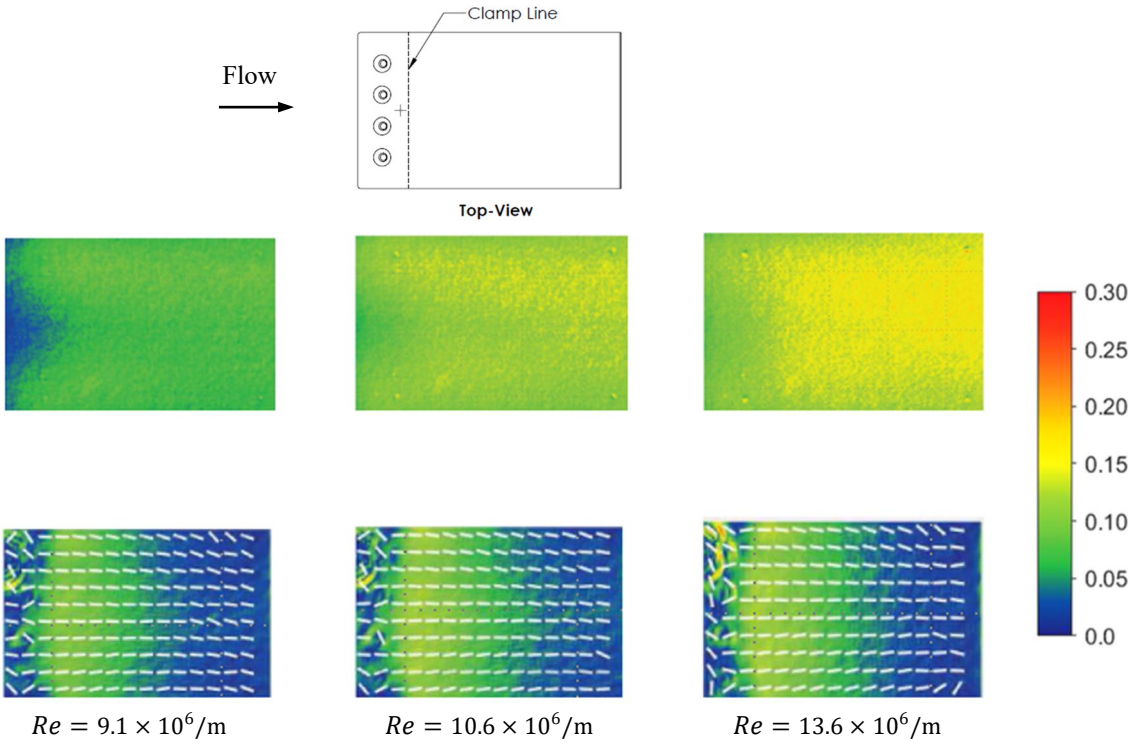

Figure 7. Uncorrected pressure ratio (top, P/P_{atm}) and optical strain response (bottom, OSR) of the flap at $t = 12$ s; flow left-to-right

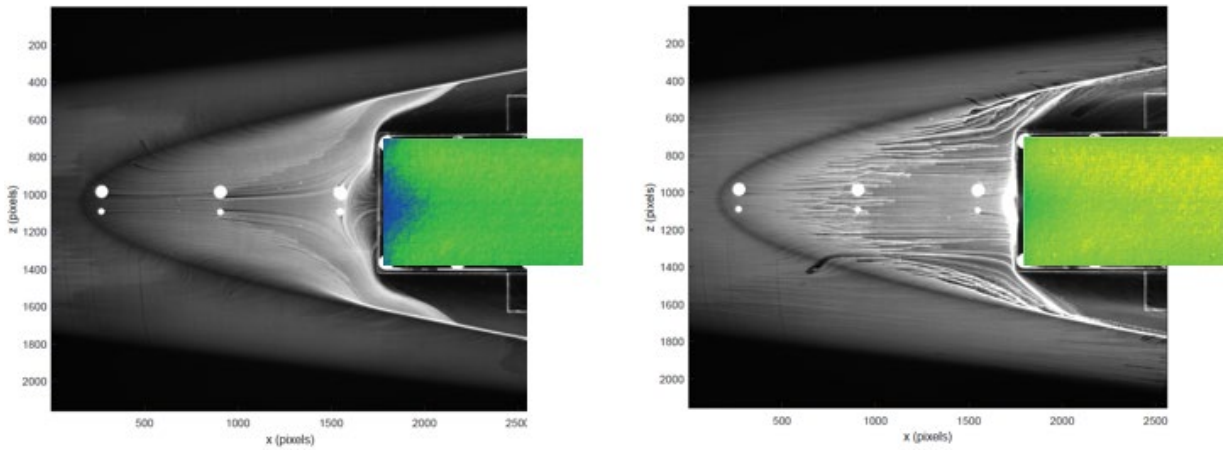

$Re = 9.1 \times 10^6/\text{m}$ $Re = 10.6 \times 10^6/\text{m}$

Figure 8. Comparison of surface oil-film results [12] and PSP results showing the separation region in front of the leading-edge of the flap

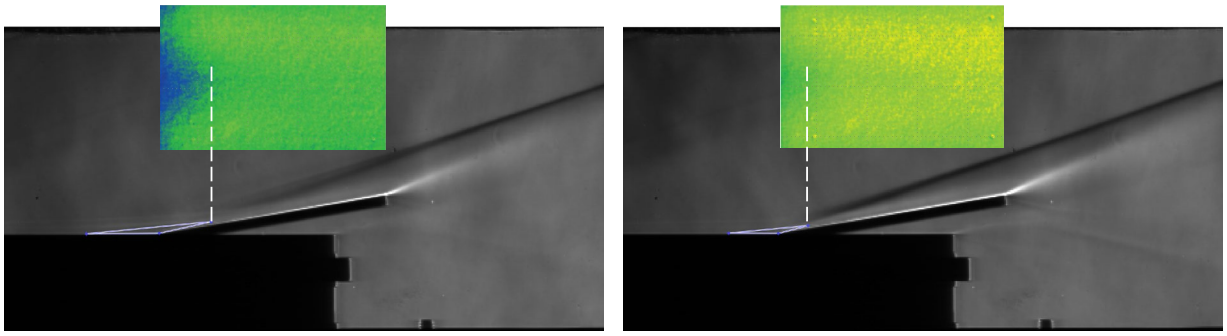

$Re = 9.1 \times 10^6/\text{m}$ $Re = 10.6 \times 10^6/\text{m}$

Figure 9. Comparison of schlieren images and PSP results showing the separation region in front of the leading-edge of the flap

PSPs are temperature sensitive. This dependency is due to both the luminophore and binder [2]. Increases in temperature will decrease the PSP emission. PECs can also exhibit temperature effects due to a change in optical sensitivity or due to thermal conductivity and expansion mismatch between the coating and the substrate. PEC optical sensitivity effects become important if the temperature approaches the glass transition value. A benchtop test to characterize temperature sensitivity was performed to compare the inverse-intensity ratio and OSR response of both the PSP (unpolarized blue excitation) and PEC (polarized red excitation). The results are plotted in Fig. 10. The PSP intensity decreases (i.e., increase in I_{ref}/I, filled blue symbols) due to increasing temperature. Because the PSP is excited with unpolarized light and the emission does not retain polarization, the PSP OSR is zero (unfilled blue symbols). Turning attention to the PEC (red symbols), temperature sensitivity is not present in the intensity ratio or OSR. The glass transition of the PEC is significantly higher than the tested range or the expected range in the tunnel. Thermal conduction and expansion effects due to PEC and substrate mismatch can play a more significant role near the edges of the coating and when flow time-scales are short relative to the thermal response. A benchtop strain test with applied weights and elevated temperature measured a temperature sensitivity of $2-3$ με/°C.

Figure 11a compares the temperature sensitivity of the custom PSP with data from a conventional PtTFPP porous paint [14], which can decrease in intensity by $2-4\%$ per °C. Both curves are fit with an exponential function to characterize the temperature sensitivity, τ, Eq. (11). The custom formulation used on the flap shows a stronger

temperature sensitivity (lower τ). As shown in Fig. 11b, the value of τ is also pressure sensitive. A temperature sensitivity calibration of the custom PSP formulation with respect to pressure is estimated by assuming the same relative sensitivity change between the two formulations at atmospheric conditions $P/P_{ref} = 1$.

$$\frac{I_{ref}}{I} = e^{\left(\frac{T}{T_{ref}}-1\right)/\tau(p)} \tag{11}$$

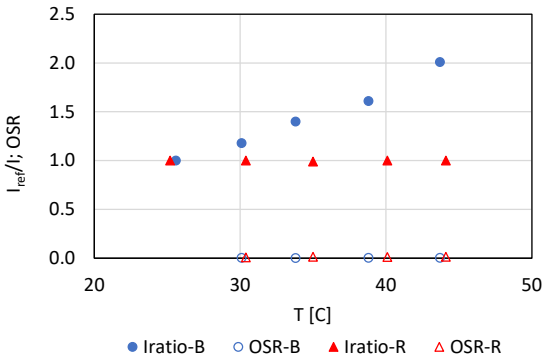

Figure 10. Temperature effect on PSP and PEC at ambient pressure

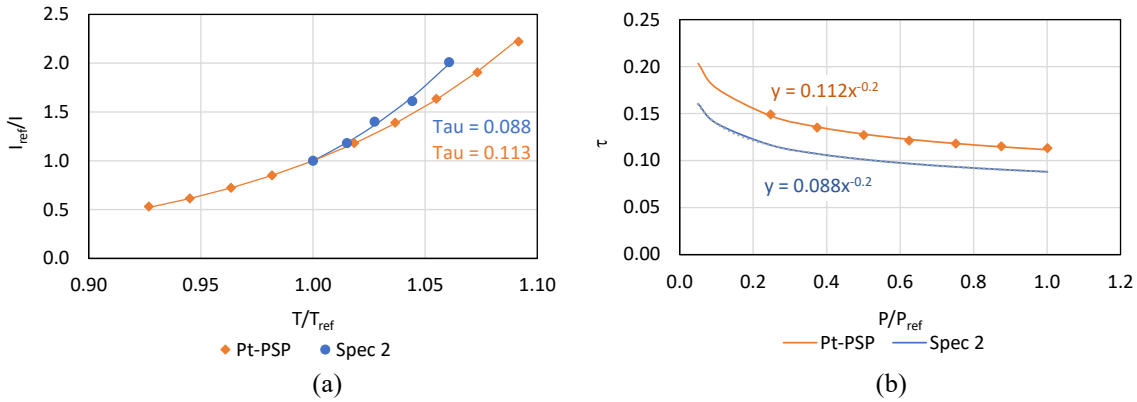

Figure 11. PSP temperature dependency: (a) comparison between a conventional PtTFPP porous paint [14] and the custom PSP (specimen 2) and (b) dependency of PSP temperature sensitivity parameter, τ, with pressure

Without the installation of surface temperature or pressure sensors on the flap, an *in-situ* temperature correction is not available. Prior temperature sensitive paint (TSP) testing was performed on a 10° wedge at similar Re but at higher stagnation temperature [11]. These results can be used to provide insight on the potential temperature rise and interference. Both the TSP insulation layer (wedge) and PEC (flap) have similar thermal properties: $k = 0.2 - 0.25$ W/(m · K) and $\alpha_T = 0.1 - 0.2$ mm^2/s. Figure 12 shows the TSP wedge results for two Re runs that match two Re run cases for the flap. After reaching the desired tunnel conditions ($3 - 4$ s after the heaters turn on), TSP images were captured for 5 s and ensemble-averaged. The average surface temperature rise for the two cases are 12 and 13 K, respectively. For the lower Re case, a small separation region exists upstream of the wedge leading edge, resulting in an area of lower temperature along the centerline of the flap near the leading edge. The higher stagnation temperature conditions for both of TSP runs would generate higher surface temperatures compared to the flap assuming other parameters were equal. TSP runs with similar stagnation temperature conditions as the flap, but at higher Re (attached flow), exhibited a more uniform temperature profile. Surface temperature increased by $6 - 7$ K. Based on the wedge

results, it would be expected that the temperature on the flap would increase once the heaters are energized and tunnel conditions are achieved. This would cause an increase in the indicated pressure over time.

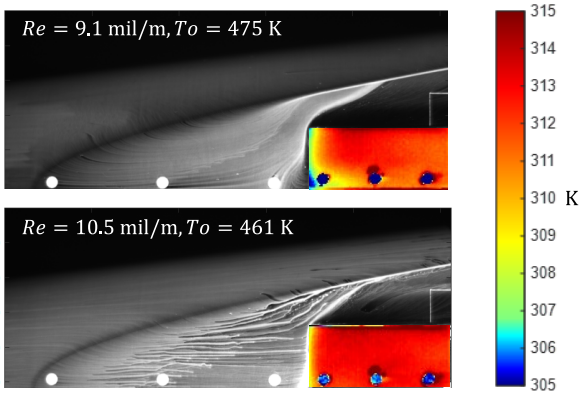

Figure 12. Oil film and TSP results for the 10° wedge

As shown previously in Fig. 6, target conditions are not reached until approximately 9 s after data acquisition is started. Figure 13a is a trace of the uncorrected pressure at the middle of the flap: 29 mm from the leading edge and along the flap centerline. The pressure and temperature rise of the tunnel are indicated by shaded blue and red regions, respectively. Temperature interference likely exists throughout the time trace. Prior to energizing the heaters, surface temperatures could cool. Then, as the stagnation temperature rises, the surface temperature would increase due to the recovery temperature being greater than the initial flap temperature. Assuming relatively small net temperature effects approaching the target conditions at $8 - 9$ s, the uncorrected pressure, as shown, would continue to increase as the tunnel stagnation pressure is approximately level. Using the fit from Fig. 11b and Eq. 11, an estimate of the temperature rise can be calculated assuming the true pressure is effectively constant. For the purpose of this calculation, the measurements at 9 s were set as the reference. The corresponding estimated temperature rise over the next 5 s for the three runs ranges from $10 - 18$ K. The width of the broad arrows on the pressure trace estimate a corrected pressure range assuming a steady surface pressure during "on" condition. Observing the corresponding maximum shear strain data, Fig. 13b, the strain peaks near $8 - 10$ s and then decreases slowly during the run. As the flap deformation is dependent on both the windward and leeward pressure distribution, higher tunnel stagnation pressure and windward surface pressure results in a higher strain.

Figure 14 plots results at a location 12 mm from the leading edge along the centerline, located near the clamp line of the flap and within the separation region for the low Re case. Again, higher stagnation pressures lead to higher surface pressures and strains. For the low Re case, the pressure trace shows less temperature interference due to the lower heat transfer. Estimated temperature interference is 2 K for the low Re run and $10 - 11$ K for the higher Re runs. The strains are higher compared to Fig. 13 as the measurement location is closer to the clamped end of the flap where the bending moment would be largest. Assuming bending is the primary mode, the principal strain for the high Re case was nominally 90 με.

B. High-speed Camera Results

Figure 15 presents the OSR and stagnation pressure traces for the complete $Re = 10.6 \times 10^6$/m run captured by the micropolarizer camera. The heaters are turned off at ~17 s and the pressure valve was shut-off at ~24 s. Closing the pressure valve causes the tunnel to unstart and subjects the model to transient loading as indicated by the spike in OSR. This loading can excite fundamental modes of the flap. Because the fundamental frequency of the flap was greater than the full-frame capture rate of the micropolarizer camera, a Phantom v2512 camera was used to acquire images at 5000 fps, approximately 10X the flap fundamental frequency. Placing a single polarizer in front of the camera lens and orienting at 45° relative to the principal strain direction, while still exciting with red circular polarized light, enables the ability to detect intensity changes due to strain-induced changes in the polarization of the PEC. PSP

data was acquired with unpolarized blue excitation. The data was captured for two runs, using an individual LED color for each run.

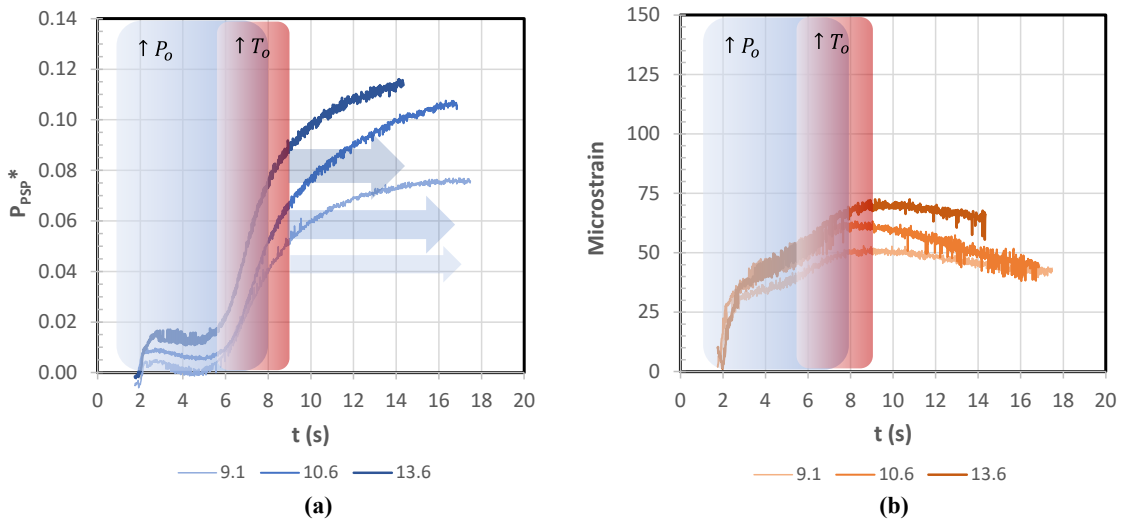

Figure 13. Pressure (uncorrected, a) and maximum shear strain (b) traces 29 mm from the flap leading and along the centerline: $9.1, 10.6$ and $13.6 \times 10^6/\mathrm{m}$

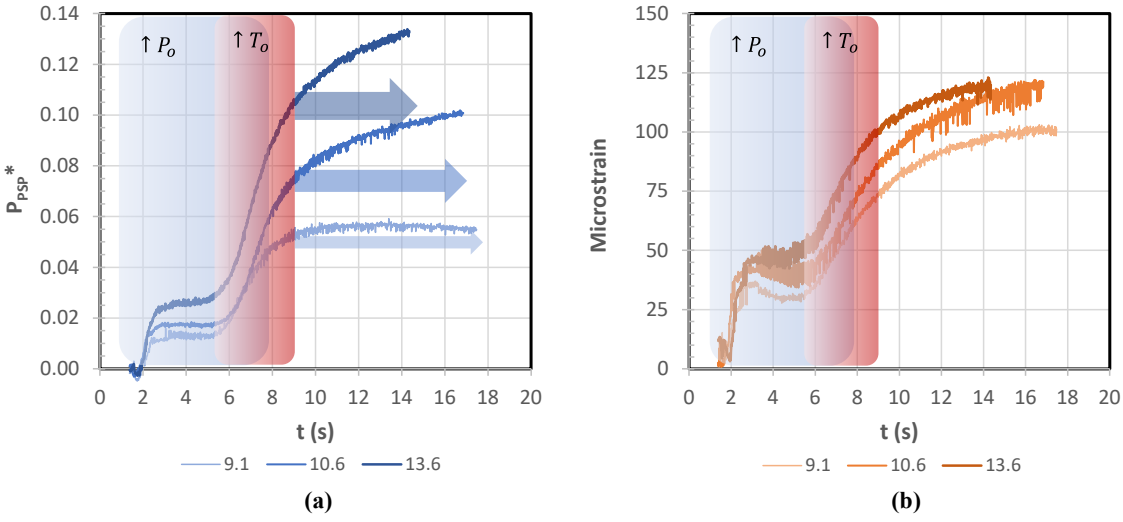

Figure 14. Pressure (uncorrected, a) and maximum shear strain (b) traces 12 mm from the flap leading and along the centerline: $9.1, 10.6$ and $13.6 \times 10^6/\mathrm{m}$

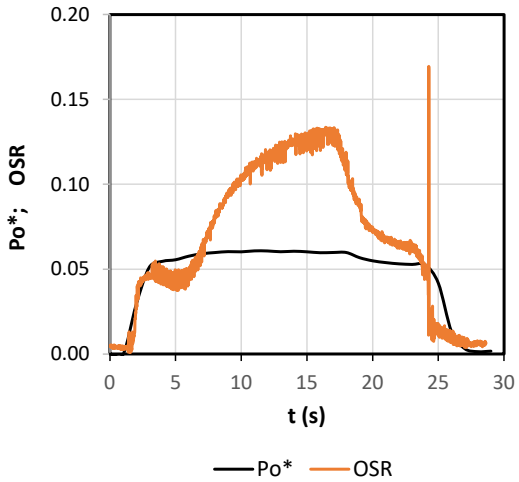

Figure 15. Stagnation pressure and OSR trace (micropolarizer camera) for $Re = 10.6 \times 10^6/\text{m}$; tunnel shut-down is at ~24 s as indicated by the spike in the OSR and decreases in stagnation pressure

Figure 16 shows intensity-ratio spectra for v2512 images captured using the red/PEC (a & b) and blue/PSP (c & d) excitation sources. Plots on the left (a & c) are during steady conditions and plots on the right (b & d) are during tunnel shutdown. Each plot includes three measurement points along the flap centerline relative to the leading-edge: 12, 29 and 46 mm. Time envelopes to calculate the spectra were approximately 0.5 s. Starting with Fig. 16a, during target tunnel conditions, the intensity from the polarized red LED captures a primary peak at 633 Hz and a secondary peak at 562 Hz. The 562 Hz corresponds with the flap/coating fundamental frequency. The driving of the 633 Hz vibration is not known. The tunnel shutdown response (Fig. 16b) shows several frequencies excited due to the transient conditions. The primary peak occurs at the fundamental frequency of the flap and is over two orders of magnitude larger than the steady state condition at the fundamental frequency. Additional peaks occur at 1115 Hz and 1560 Hz. While the spectra magnitude cannot be calibrated to OSR as a full-set of polarized states were not captured, the response would be related to strain: higher amplitudes corresponding to higher strains. The spectra associated with the blue LED and PSP (c & d) do not show distinct peaks associated with flap vibration except for a small peak at the fundamental frequency (marked with an arrow in Fig. 16d) . The overall broadband amplitude and noise floor increases for the shutdown case due to the sudden increase in pressure.

Figure 17 plots the spectra amplitude (a, rainbow contours) and effective phase (b, red-blue contours) over the flap at the 562 Hz and 1560 Hz. The rainbow contours are related to the maximum shear strain and the red-blue contours are related to principal direction, though neither are directly measured as only a single polarizer is placed in front of the camera. At 562 Hz, contours show the first symmetric bending mode of the clamped flap. The highest strain is near the clamp line and then decreases towards the trailing edge, similar to the OSR plots (Fig. 7). The minor spanwise asymmetry may be due to the inability to account for the reference birefringence in the coating using a single polarizer. The 1560 Hz contour shows the first antisymmetric mode due to torsion. The longitudinal symmetry of the rainbow color contour for this case (Fig. 17a, 1560 Hz) is because the measurement is related to the maximum shear strain and not the flap deformation or principal strain. The torsional nature of this mode is visible in the phase plot (Fig. 17 b, 1560 Hz) where the red and blue colors are related to orthogonal principal strain directions. The frequency ratio of the torsional mode to the bending mode is 2.78. The effective aspect ratio for the flap is 1.15 (51 mm /44.5 mm). For a square clamped flap (1:1), the ratio of modes is 2.45 [16], further supporting the torsional nature of the 1560 Hz contour. Referring back to Fig. 16b, a vibration peak occurs at 1115 Hz. While the corresponding contours are not shown in Fig. 17, this is a harmonic of the fundamental bending mode, and the contours are qualitatively similar to that of 562 Hz except being lower in magnitude.

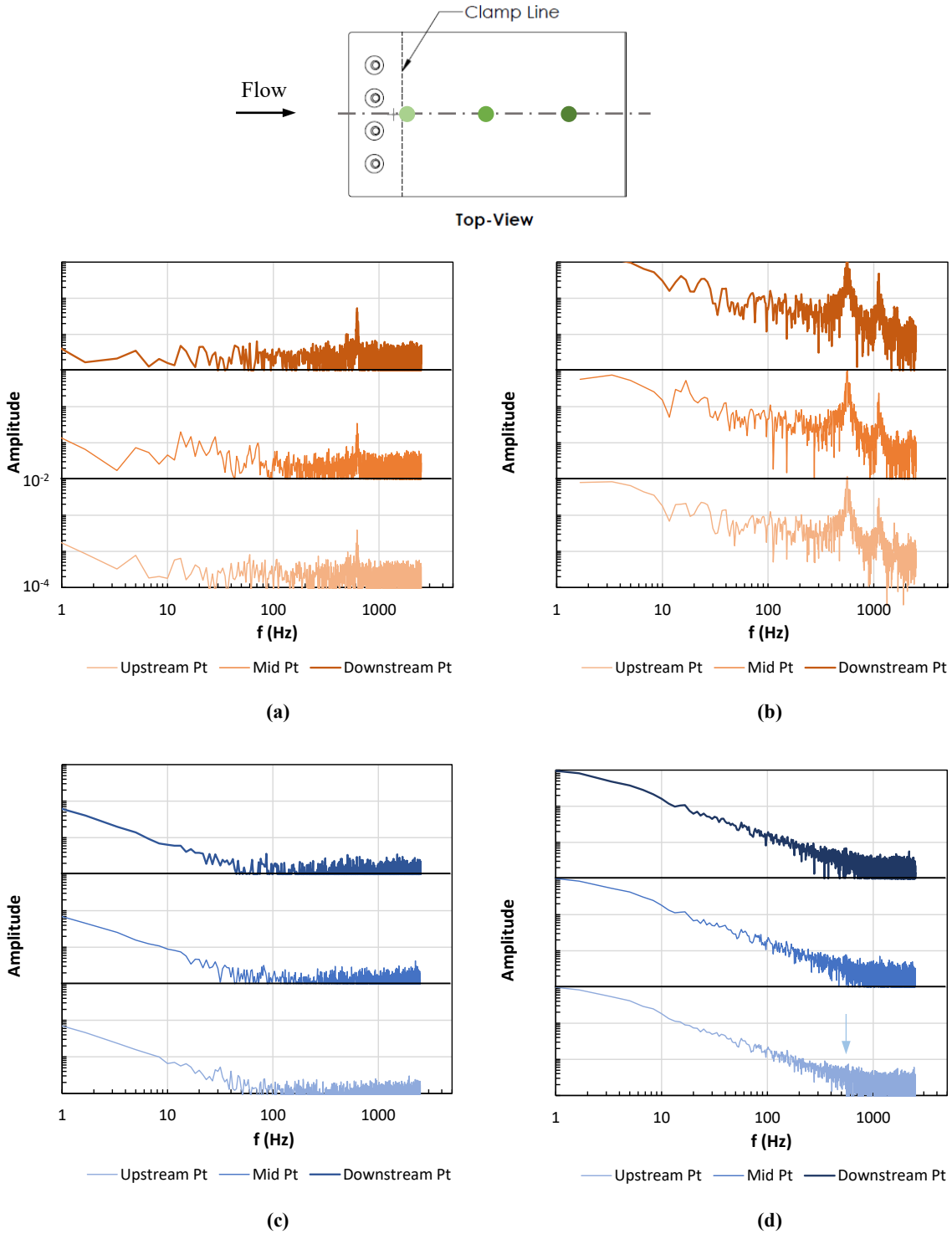

Figure 16. Intensity-ratio spectra for the red (a & b) and blue (c & d) excitation of the PEC and PSP coating at three locations: 12, 29 and 46 mm from the flap leading edge (bottom to top of each image, respectively); left plots (a & c) are for steady run conditions and right plots (b & d) are during tunnel shutdown: $Re = 13.1 \times 10^6/\mathrm{m}$

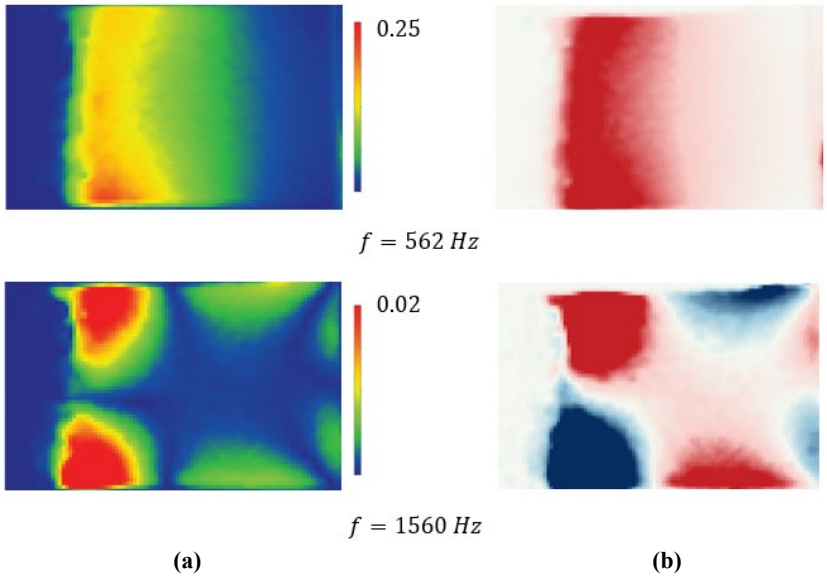

Figure 17. Spectra amplitude (a) and effective phase (b) contours at 562 Hz and 1560 Hz using the high-speed camera and a single polarizer; the rainbow contours are related to the maximum shear strain and the red-blue contours are related to principal direction

V. **Conclusions**

A dual-layer pressure and strain measurement technique using a custom pressure-sensitive paint and a commercial photoelastic underlayer was tested on a 10° flap attached to a slender cone-slice model (Mach 5, $Re = 9 - 14 \times 10^6/\mathrm{m}$). The coating was excited using two, strobed, high-powered blue/UV (405 nm, unpolarized) and red (620 nm, circular polarized) LED lights. Images were acquired using a digital camera with a micropolarizer mask as well as a high-speed digital camera with a linear polarizer. The test was a culminating task of a project to research and develop the technique for high-speed, fluid-structure interaction environments. Conclusions from the investigation are:

- The average intensity measurements over the four-polarizer angles for each superpixel were converted to pressure using a pseudo-*in situ* calibration. Prior to a test run, images were acquired at atmospheric and vacuum conditions to obtain a two-point calibration. The resulting surface pressure contours, uncorrected for aerodynamic heating, captured the effects of flow separation upstream of the flap at the lower Re condition. This matched the size and extent of the separated region measured using schlieren imaging and oil-film visualization (the latter on a 10° wedge). Higher stagnation pressure (and Re) conditions resulted in higher pressure on the windward side of the flap. Surface heating during the run affects the pressure measurement due to inherent PSP temperature sensitivity and the insulating nature of the PEC. This likely results in an overestimation of pressure as the run progresses. The estimated surface temperature rise, based on the PSP temperature sensitivity and assuming a constant surface pressure after target conditions were reached, ranged from 2 K (low Re, separated region) to upwards of 18 K at the center of the flap. For long run facilities, temperature correction will be necessary and could potentially be achieved with a TSP/PEC or TSP coated model tested at the same conditions or calibrating with *in situ* surface pressure sensors. The latter approach would require special care in regard to the PEC application with surface pressure sensors.
- The standard deviation of intensity measurements over the four-polarizer angles for each superpixel were converted to maximum shear strain by correcting for the coating birefringence at the reference state and using an *a priori* calibration from prior tests. As expected, during target run conditions, the strain magnitude was well below the yield value of the material. The strain increased with tunnel stagnation pressure and decreased from the clamped end of the flap to the free trailing-edge. The corresponding principal direction was predominately

parallel to the longitudinal axis of the flap which is expected for a cantilever plate in bending. Strain measurements did not settle to a constant value once the tunnel target conditions were attained, particularly near the clamped end of the flap. Temperature sensitivity of the PEC applied to the flap was measured to be $2-3\ \mu\varepsilon/°\mathrm{C}$ and, thus, could account for some of the drift. Thermally induced strain near the clamped boundary could also play a role.

- High-speed camera results (without a micropolarizer mask) were able to capture the resonant structural frequency of the coated flap when excited by the shutdown transients of the tunnel. Both the first bending (562 Hz) and torsional (1560 Hz) modes were captured. The peak at 1115 Hz (of lower amplitude) is a harmonic of the first bending mode. The PEC application did increase the flap resonant frequency by 22%. Thus, for thin structures, a thinner coating is preferred. In this experiment, the thinnest pre-fabricated sheet was used. The trade-off of a thinner coating would be less strain sensitivity and potentially the need for an alternative application approach. Frequency peaks, fluidic or structural, were not captured in the pressure spectra except for a small peak at the first bending mode during shutdown. Peaks at low frequency were not expected. Because the PSP temporal response was measured at $\sim 2\ ms$, pressure response due to structural vibration would be attenuated at higher frequencies. The slower PSP response compared to other developed fast-PSPs is due to the lower concentration of porous media in the binder. While higher concentration increases response times, it decreases the excitation polarization and corresponding strain sensitivity; thus, there is a need to balance between the two. For both the strain and pressure spectra, broadband energy was higher for shutdown conditions compared to steady run conditions. While strain was not directly measured (the PEC reflection was captured at a single polarization orientation), the results show the capability to measure strain at higher frequencies. This requires a high-speed camera with a micropolarizer mask (four polarization orientations), high polarization extinction ratio, and high quantum efficiency at the required wavelength, as well as high-powered LED sources.
- During the tunnel entry, nine runs were performed on one of the PSP/PEC coated flaps. Little degradation or damage to the coating was noticed when monitoring the emission intensity and inspecting the model between runs.
- The test demonstrated the viability and current limitations of the approach, highlighting areas that need further research and development to advance the technique. These areas include, but are not limited, to temperature correction procedures (especially for long runs) to account for temperature sensitivity, approaches to improve dynamic pressure response without adversely affecting strain sensitivity, application of thinner and alternative coatings sensitive to strain-induced polarization changes to reduce structural stiffening, and the development of PSPs that could retain a high-degree of polarization upon emission, eliminating the need for the red LED and using only a circular polarized blue/UV LED.

VI. Acknowledgments

This project is supported by NSF and AFOSR Grant CBET-180299: program managers Dr. Ronald Joslin and Dr. Sarah Popkin. The authors also like to thank Dr. J. Crafton and Ms. C. Ryan of ISSI for PSP consultation, development, and application as well as the engineering and technical staff at Sandia's Hypersonic Wind Tunnel including Russell Spillers, Raj Bhakta, Marie De Zetter, and Kyle Daniel. Sandia National Laboratories is a multi-mission laboratory managed and operated by National Technology and Engineering Solutions of Sandia, LLC., a wholly owned subsidiary of Honeywell International, Inc., for the U.S. Department of Energy's National Nuclear Security Administration under contract DE-NA0003525. The views expressed in the article do not necessarily represent the views of the U.S. Department of Energy or the United States Government.

References

[1] Flaherty, WP, T Reedy, GS Elliot, JM Austin, RF Schmit, and JW Crafton, "Investigation of Cavity Flow Using Fast Response Pressure Sensitive Paint," *AIAA Journal*, Vol. 52, No. 11, 2014, pp 2462-2470.

[2] Liu, T, and JP Sullivan, *Pressure and Temperature Sensitive Paints,* Springer-Verlag, Berlin, 2004.

[3] Zandman, FS Redner, and JW Dally, *Photoelastic Coatings*, Iowa State University Press, Ames, IA, 1977.

[4] Hubner, JP, A Hegde, K Chism, S Ölçmen, and J Crafton, “Full-field Pressure and Strain Measurement Technique using a Dual-Layer Luminescent Coating,” *AIAA Journal*, Vol. 59, No. 5, 2020, pp. 1517-1527, DOI: 10.2514/1.J060058.

[5] Hegde, A, M Chen, S Ölçmen, JP Hubner, J Crafton, and C Ryan, “Pressure and Strain Measurement on a Thin Clamped Plate in Supersonic Flow using a Dual-Layer Luminescent Coating,” AIAA Aviation Forum, AIAA Paper 2021-2920, August 2021, DOI 10.2514/6.2021-2920.

[6] Martellucci, A, and S Weinberg, “MAT Program Test Summary Report. Biconic Body with Slice/Flap,” Technical Report ADA118242, 1982, https://apps.dtic.mil/sti/citations/ADA118242.

[7] Oberkampf, WL, and DP Aeschliman, “Joint computational/experimental aerodynamics research on a hypersonic vehicle Part 1: Experimental results,” *AIAA Journal*, Vol. 30, No. 8, 1992, pp. 2000–2009, DOI:10.2514/3.11172.

[8] Dolling, DS, "Fifty Years of Shock-wave/Boundary Layer Interaction Research:What Next?," *AIAA Journal,* Vol. 39, No. 8, 2001, pp. 1517-1531.

[9] Zheltovodov, AA, "Some Advances in Research of Shock-wave Turbulent Boundary Layer Interactions," 44th AIAA Aerospace Sciences Meeting and Exhibit*,* AIAA Paper 2006-496, January 2006.

[10] Gaitonde, DV, “Progress in Shock Wave/Boundary Layer Interactions,” AIAA 43rd Fluid Dynamics Conference, AIAA Paper 2013-2607, June 2013.

[11] Pandey, A, KM Casper, R Spillers, M Soehnel, and S Spitzer, “Hypersonic Shock Wave-Boundary Layer Interaction on the Control Surface of a Slender Cone,” AIAA SciTech Forum, AIAA Paper 2020-0815, January 2020.

[12] Pandey, A, KM Casper, M Soehnel, R Spillers, R Bhakta, and SJ Beresh, “Hypersonic Fluid-Structure Interaction on the Control Surface of a Slender Cone,” AIAA SciTech Forum, AIAA Paper 2021-0909, January 2021.

[13] Application Note B-223, “Instructions for Bonding Flat and Contoured Photostress Sheets,” Micro-Measurements, Rayleigh, NC, March 2017.

[14] “Porous, Fast Responsive Pressure Sensitive Paint: FP-XXX,” Innovative Scientific Solutions, Inc., Dayton, OH.

[15] Tech Note TN-706-1, “Corrections to Photoelastic Coating Fringe-Order Measurements,” Micro-Measurements, Rayleigh, NC, August 2015.

[16] Young, D, “Vibration of Rectangular Plates by the Ritz Method,” *Journal of Applied Mechanics*, Vol. 17, No. 4 pp. 448-453, 1950.